INTERNATIONAL JOURNAL FOR NUMERICAL METHODS IN FLUIDS, VOL. 7, 155–173 (1987)

SOLUTION OF THREE-DIMENSIONAL NATURAL CONVECTION ABOUT A VERTICAL SQUARE ROD IN A CYLINDRICAL ENCLOSURE

E. K. GLAKPE, C. B. WATKINS, JR. AND B. KURIEN

Department of Mechanical Engineering, Howard University, Washington, D.C. 20059, U.S.A.

SUMMARY

The problem of three-dimensional laminar natural convection in a vertical enclosure with an inner square rod is treated by a numerical method in boundary-fitted co-ordinates. The inner and outer cylinders are heated and cooled, respectively, to maintain different constant surface temperatures. The horizontal enclosure surfaces are maintained at adiabatic conditions. The Prandtl number is that of air, 0·703, and the Rayleigh numbers span the conduction, transition and boundary layer regimes of flow. The radius ratio is 1, and the aspect ratio (cylinder length divided by maximum annular gap) is 1. The results of the study provide data useful in the design and performance assessment of nuclear reactor spent fuel shipping casks.

KEY WORDS Cavity Flow Three-dimensional Primitive Variables Navier–Stokes Equations Boundary-fitted Co-ordinates SIMPLE Solution Scheme

INTRODUCTION

Numerical computation of three-dimensional natural convection in an enclosure is still far from routine, but it has important practical applications. Energy-related applications have stimulated much of the current interest in this area. Some specific application areas include compact electronic packaging, nuclear reactor safety, shipping containers for spent nuclear fuel, residential heating and cooling and heat removal from transformers in power plant applications. A configuration of practical importance that simulates a type of shipping container for the transportation of spent fuel is a vertical enclosure consisting of an inner square rod bounded by a circular enclosure. This geometry is also of interest in the pool storage of spent fuel. The natural convection flow phenomenon in this enclosure geometry is three-dimensional in nature and, numerically, involves the simultaneous solution of the three-dimensional Navier–Stokes and energy equations.

Natural convection in a cylindrical annulus configuration has attracted a significant amount of attention, and a review of the studies involving this geometry was presented by Kuehn and Goldstein.[1] However, most of the studies reported were for horizontal concentric cylinders with infinite axial length, enabling the convective flow to be regarded as two dimensional.

Recent improvements in the processing speed and memory capacity of digital computers have placed numerical computation of three-dimensional natural convection within reach of many investigators. Several such numerical studies have been reported, mostly for rectangular enclosures. Aziz and Hellums[2] obtained numerical solutions to the transient governing equations for a rectangular configuration by means of an alternating direction implicit (ADI) method.

0271–2091/87/020155–19$09.50

Received 14 May 1986

Their main objective was to demonstrate the feasibility of using a vector potential in the transformation of the governing flow equations. Mallinson and Davis[3,4] developed the false transient method and applied it to the problem of three-dimensional natural convection in a box, employing similar formulations of the governing equations. To avoid certain problems involved in the numerical representations of boundary conditions in the approach of previous investigators,[3,5] Chan and Banerjee[6] adopted a different approach. They developed a numerical technique based on the marker and cell (MAC) method of Harlow and Welch,[7] applying it to the analysis of three-dimensional natural convection in a rectangular enclosure.

Only a limited number of computational studies have been reported on natural convection in concentric cylindrical annuli that necessitated solution of the three-dimensional Navier–Stokes and energy equations. In studying the ducting system of a high-temperature gas-cooled reactor (HTGR), Takata *et al.*[8] obtained numerical solutions to the natural convection in a vertical curved annulus containing porous material. In later work[9] they reported solutions to the natural convection problem in an inclined concentric cylindrical annulus. In both cases the vorticity–vector-potential formulations of the governing equations were used. To eliminate the pressure terms in the Navier–Stokes equations, Tolpadi and Kuehn[10] also used a similar approach in studying conjugate conduction–natural-convection heat transfer from a horizontal isothermal cylinder with fins. Like their predecessors,[2,8,9] they used an ADI scheme to solve the parabolic part of the problem, i.e. the temperature and vorticity transport equations, and a successive over-relaxation method was used for the elliptic problem, i.e. the vector potential equations.

The purpose of the present paper is to describe heat transfer and flow field solutions for the natural convection problem in a vertical enclosure for which the inner and outer cylinders are heated and cooled, respectively, to maintain different constant surface temperatures. The horizontal surfaces are assumed adiabatic. The Prandtl number is that of air, 0·703, and the Rayleigh number ranges from 0 to 10^6. The radius and aspect ratios are fixed at the value of 1. The numerical solutions to the flow equations are obtained in a boundary-fitted co-ordinate system following the approach taken by Chen *et al.*[11] as modified recently by the present authors for a two-dimensional problem[12] and extended to three dimensions herein.

NUMERICAL SOLUTION

As indicated in the previous section, most of the numerical studies on three-dimensional natural convection have been based on the vorticity–vector-potential formulation of the governing equations. The attractive feature of this approach is that the pressure is eliminated from the momentum equations and the continuity equation is automatically satisfied by the definition of the vector potential. However, by using this approach, the number of unknowns becomes seven, namely the three components of the vorticity vector, the three components of the vector potential and temperature. It is also difficult numerically to specify the boundary conditions for vorticity. In order to avoid these complications, the present three-dimensional study is based on the primitive variables form of the governing equations.

The finite-difference grid system

The co-ordinate system adopted for the present study is based on the boundary-fitted curvilinear co-ordinate transformation algorithm of Thompson.[13] The basic idea is numerically to generate a curvilinear co-ordinate system having co-ordinate lines coincident with each boundary of the physical region of interest. This approach enables accurate numerical representations of the boundary conditions to be accomplished without resorting to interpolative schemes that reduce

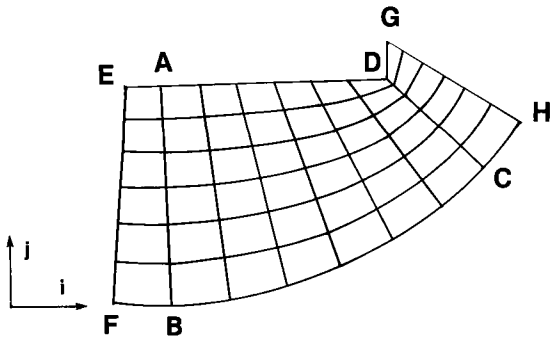

Figure 1. Grid distribution in boundary-fitted co-ordinates

the accuracies of the numerical approximations for physical variables of interest.

The co-ordinate system is generated by solving the following system of elliptic equations:

$$\alpha x_{\xi\xi} - 2\beta x_{\xi\eta} + \gamma x_{\eta\eta} + J^2[x_\xi P(\xi,\eta) + x_\eta Q(\xi,\eta)] = 0, \tag{1}$$

$$\alpha y_{\xi\xi} - 2\beta y_{\xi\eta} + \gamma y_{\eta\eta} + J^2[y_\xi P(\xi,\eta) + y_\eta Q(\xi,\eta)] = 0, \tag{2}$$

where the transformation coefficients and Jacobian are defined by the following relationships:

$$\alpha = x_\eta^2 + y_\eta^2, \quad \gamma = x_\xi^2 + y_\xi^2,$$
$$\beta = x_\xi x_\eta + y_\xi y_\eta, \quad J = x_\xi y_\eta - x_\eta y_\xi.$$

By specifying Dirichlet conditions on the boundaries, a grid system composed of (x, y) values corresponding to discrete values of ξ and η is generated. The functions P and Q in equations (1) and (2) are co-ordinate control functions that may be used to cause the co-ordinate lines to concentrate in certain parts of the region of interest.

The present work uses a three-dimensional co-ordinate system for which the curvilinear co-ordinates in the plane normal to the enclosure axis are generated from equations (1) and (2) and the third (axial) co-ordinate is linearly transformed in the axial direction. The resultant grid distribution is shown in Figure 1 for one-eighth of the enclosure in a plane normal to the vertical axis. For later reference, grid lines next to the symmetry lines AB and DC are also shown in this figure.

Transformed governing equations

The dimensionless forms of the transformed governing equations as they appear in Reference 11 are given as follows:

Continuity equation.

$$\int_V J\rho_t \,\mathrm{d}V + \int_{S_\xi} \rho\tilde{u}\frac{1}{a}\,\mathrm{d}\eta\,\mathrm{d}\zeta + \int_{S_\eta} \rho\tilde{v}\frac{1}{a}\,\mathrm{d}\xi\,\mathrm{d}\zeta + \int_{S_\zeta} \rho\tilde{w}J_{12}\,\mathrm{d}\xi\,\mathrm{d}\eta = 0. \tag{3}$$

x-momentum equation.

$$\int_V Ja(\rho u)_t \,\mathrm{d}V + \int_{S_\xi} \rho u\tilde{u}\,\mathrm{d}\eta\,\mathrm{d}\zeta + \int_{S_\eta} \rho u\tilde{v}\,\mathrm{d}\xi\,\mathrm{d}\zeta$$

$$+\int_{S_\zeta} aJ_{12}\rho u\tilde{w}\,d\xi\,d\eta = -\int_{S_\zeta} y_\eta p\,d\eta\,d\zeta + \int_{S_\zeta} y_\xi p\,d\xi\,d\zeta$$
$$+\int_{S_\zeta} \tilde{\Sigma}_{11}\,d\eta\,d\zeta + \int_{S_\eta} \tilde{\Sigma}_{12}\,d\xi\,d\zeta + \int_{S_\zeta} aJ_{12}\tilde{\Sigma}_{13}\,d\xi\,d\eta. \tag{4}$$

y-momentum equation.

$$\int_V aJ(\rho v)_t\,dV + \int_{S_\xi} \rho v\tilde{u}\,d\xi\,d\zeta + \int_{S_\eta} \rho v\tilde{v}\,d\xi\,d\zeta$$
$$+\int_{S_\zeta} aJ_{12}\rho v\tilde{w}\,d\xi\,d\eta = \int_{S_\zeta} x_\eta p\,d\eta\,d\zeta - \int_{S_\eta} x_\xi p\,d\xi\,d\zeta \tag{5}$$
$$+\int_{S_\zeta} \tilde{\Sigma}_{21}\,d\eta\,d\zeta + \int_{S_\eta} \tilde{\Sigma}_{22}\,d\xi\,d\zeta + \int_{S_\zeta} aJ_{12}\tilde{\Sigma}_{23}\,d\xi\,d\eta.$$

z-momentum equation.

$$\int_V aJ(\rho w)_t\,dV + \int_{S_\zeta} \rho w\tilde{u}\,d\eta\,d\zeta + \int_{S_\eta} \rho w\tilde{v}\,d\xi\,d\zeta$$
$$+\int_{S_\zeta} aJ_{12}\rho w\tilde{w}\,d\xi\,d\eta = -\int_{S_\zeta} aJ_{12}p\,d\xi\,d\eta \tag{6}$$
$$+\int_{S_\zeta} \tilde{\Sigma}_{31}\,d\eta\,d\zeta + \int_{S_\eta} \tilde{\Sigma}_{32}\,d\xi\,d\zeta + \int_{S_\zeta} aJ_{12}\tilde{\Sigma}_{33}\,d\xi\,d\eta + \frac{1}{F^2}\int_V Ja(\rho - \rho_s)g\,dV,$$

where $F = gL^3/\nu^2$.

Energy equation.

$$\int_V Ja(\rho h)_t\,dV + \int_{S_\zeta} \rho h\tilde{u}\,d\eta\,d\zeta + \int_{S_\eta} \rho h\tilde{v}\,d\xi\,d\zeta$$
$$+\int_{S_\zeta} aJ_{12}\rho h\tilde{w}\,d\xi\,d\eta + \frac{1}{Pr}\int_{S_\zeta} \tilde{q}_1\,d\eta\,d\zeta \tag{7}$$
$$+\frac{1}{Pr}\int_{S_\eta} \tilde{q}_2\,d\xi\,d\zeta + \frac{1}{Pr}\int_{S_\zeta} aJ_{12}\tilde{q}_3\,d\xi\,d\eta = 0.$$

In the above equations, S_ξ and S_η represent the two control volume surfaces of constant ξ and η, respectively; V is the volume element bounded by these surfaces. Viscous dissipation and work done by other external forces have been neglected in the energy equation. The Boussinesq approximation

$$\rho = \rho_0[1 - \beta_0(T - T_0)] \tag{8}$$

is employed in expressing the body force term in the z-momentum equation as a linear function of the temperature. The equation of state is that of a perfect gas, which in dimensionless terms becomes

$$T = h. \tag{9}$$

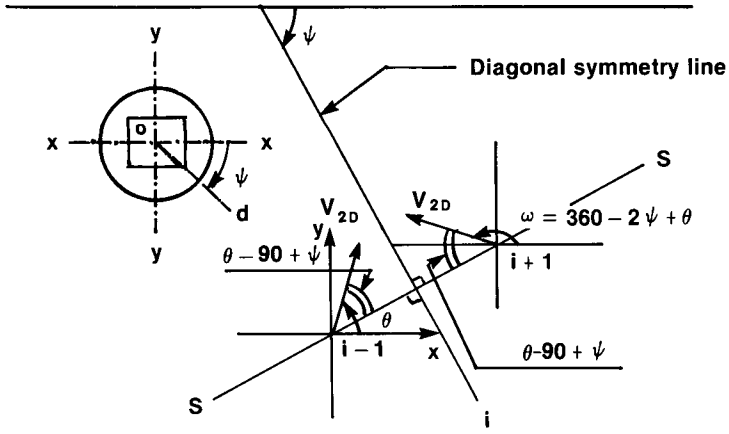

Figure 2. Notation used in formulating boundary conditions along the diagonal symmetry line

The relationships between variables in the transformed and physical regions are given in Reference 11. Subject to the boundary and initial conditions, the above equations, from which the pressure, velocity and temperature distributions can be determined, completely describe the flow field.

Boundary and initial conditions

The inner and outer walls, and the top and bottom horizontal surfaces are modelled as no-slip surfaces; hence the velocity components u, v and w are set equal to zero along these surfaces. Owing to the nature of the natural convection problem under investigation, the solution to the governing equations is sought for in an eighth of the entire planar region. As shown in Figure 2, the solution domain is bounded by the symmetry lines 0–y, the diagonal lines 0–d, and the inner and outer cylindrical surfaces.

To set the boundary conditions along the symmetry lines, the reflection method of Reference 14 is employed. Extra grid lines EF and GH denoted by $i-1$ and $i+1$, respectively, in Figure 1 are defined in order to exercise this method. Since the symmetry line AB (denoted by i) lies on the y-axis of the physical geometry,

$$u_{i-1} = -u_{i+1} \tag{10}$$

and

$$f_{i-1} = f_{i+1}, \quad \text{for} \quad f = v, w, p \text{ or } h. \tag{11}$$

These conditions model the antisymmetric reflection of the u-velocity and the symmetric reflection of the other variables. In the above equations, u_{i-1} and v_{i-1} are the velocity components along EF that are normal and tangential (parallel), respectively, to the symmetry line AB.

The boundary conditions on the u and v velocities along the symmetry line DC (denoted by i) are not as easily set as is the case along AB. With reference to Figure 2, the 'reflected' velocity components along GH are related to the computed velocity components along the $i-1$ grid line through the following relationships:

$$u_{i+1} = (V_{2D})_{i-1} \cos \omega$$
$$v_{i+1} = (V_{2D})_{i-1} \sin \omega$$

where

$$(V_{2D})_{i-1} = (u_{i-1}^2 + v_{i-1}^2)^{1/2}$$
$$\omega = 2\pi - 2\psi + \theta$$

and θ is the angle that the resultant velocity $(V_{2D})_{i-1}$ makes with the positive x-direction. Symmetric reflection of the other variables is accomplished with equations similar to equation (11).

The top and bottom surfaces are kept adiabatic, implying that

$$\frac{\partial T}{\partial z} = 0, \quad \text{for } z = 0 \text{ or } H,$$

and the inner and outer boundaries are maintained isothermal at T_h and T_c respectively. Initially, the fluid is stationary at a uniform temperature and pressure of atmospheric conditions. All constant property values are evaluated at the arithmetic mean value of T_h and T_c.

MODIFIED SOLUTION METHOD

A staggered mesh system is adopted for the derivations and solution of the finite difference approximation to the integral flux equations. Details of most of the derivations can be found in Reference 11. The velocities are computed at the intersections of the numerically generated grid lines, and the other variables are computed and stored in the centre of the cell formed by the grid lines. One of the advantages of this approach is to avoid specifying pressure conditions at the boundaries.

The SIMPLE scheme of Patankar[15] is programmed to solve the finite difference equations resulting from the discretization. The algorithm requires that a pressure correction equation be derived and solved at each iteration level of the solution procedure. Details of the derivation of the pressure correction equation in a boundary-fitted coordinate system can be found in Reference 16. The resulting equation at each computational node can be cast in the form

$$\sum_{l=1}^{9} \sum_{k=1}^{3} a_{lk} p'_{lk} + S = 0, \tag{12}$$

in which S is the source term equal to the residual mass obtained from the finite-differenced continuity equation with a velocity field that does not satisfy the continuity equation. The derivation of the discretized equation for S in a boundary-fitted staggered mesh is also contained in Reference 16.

For a specified Rayleigh number, the SIMPLE algorithm is exercised in solving the resulting finite-difference equations in a time-marching manner until a steady state is achieved. Each iteration within a time step is equivalent to one sweep of the algorithm. The SOR iterative scheme is employed for the solution of the momentum, energy and pressure correction equations. At each iteration, the momentum equations are solved first, followed by the pressure correction equation. The pressure and the velocities are 'corrected' before the solution to the energy equation is obtained. The pressure correction equation at a node involves twenty-six other neighbouring computational nodes. To reduce the amount of computational work involved, the contributions to the pressure correction equation from nodes at axial levels $k-1$ and $k+1$ were set equal to zero, prior to the iteration for p' at axial level k. Furthermore, to avoid divergence, it was found necessary to set the initial guess values for p' as zero at the beginning of the inner iteration loop for the pressure correction values.

It should be noted that in the original method[11] the contributions to the pressure-correction

equation of all neighbouring nodes are neglected, and no corrections are added to the velocities with the resultant pressure corrections. The modifications reported herein have been found to improve the convergence of the numerical scheme.

RESULTS AND DISCUSSION

Numerical results have been obtained for the enclosure problem in a Rayleigh number range of 0 to 10^6. The Prandtl number was fixed at 0·703, and the enclosure radius and aspect ratios kept constant at one. In employing the SIMPLE scheme to solve the finite-differenced governing equations, the pressure correction equations were solved in an inner loop of each iteration with the SOR scheme. In spite of the modifications to the solution scheme, the performance of the scheme was not particularly good, and was extremely sensitive to the relaxation parameters employed. One of the reasons for the slow convergence rate may be the truncation of some terms of the pressure correction equations.

All numerical computations were carried out using the Howard University's IBM 3033s computing facility. The majority of the computations were performed with a grid distribution of IMAX = 9 in the angular direction, JMAX = 15 in the radial direction and KMAX = 7 in the axial direction. It should be mentioned that because of the staggered mesh employed, a finer grid distribution, equivalent to JMAX = 30, is obtained for the evaluation of wall temperature gradients. To obtain a converged solution of the numerical scheme, it was required that the maximum absolute changes in the flow variables between consecutive iterations be less than 10^{-4}. Additionally, the residues of mass continuity and the other equations were required to be less than 10^{-4} and 10^{-3}, respectively.

For a grid distribution of $9 \times 15 \times 7$, the central processing unit time on the IBM 3033S was about 12 for each iteration. To speed up convergence at a given Rayleigh number, the computation was commenced with input data derived from a previous lower Rayleigh number calculation. The iterations were performed in a time marching manner and since an implicit finite difference method was employed, there was no restriction on the time step used. Without under-relaxation of the flow variables, the numerical procedure would not converge. A range of relaxation factors (0·3–1·0) was therefore applied. A steady state was achieved when the number of iterations required for a converged solution within a time step was less than or equal to 3.

To establish grid-independent results, several grid distributions were tested. The refinement of the grid system from $9 \times 7 \times 7$ to $9 \times 11 \times 7$ produced differences of 3·8 per cent and 11·2 per cent in the average Nusselt number for $Ra = 10^5$, respectively. Further refinement to a $9 \times 15 \times 7$ system produced changes of 0·9 per cent and 2·9 per cent for the same Rayleigh numbers. The trend in the average Nusselt number on grid refinement is depicted in Figure 3 and, as expected, the Nusselt number achieves an asymptotic value as the total number of grid points is increased.

Owing to the non-existence of published results on the enclosure geometry of interest, it was not possible directly to assess the accuracy of the present results. However, to demonstrate the validity and reliability of the scheme for producing meaningful and accurate results, test calculations were performed on a coaxial vertical cylinder arrangement studied by other investigators.[17–19] The inner and outer cylinders were maintained at different constant temperatures with adiabatic conditions on the horizontal surfaces.

Results for the test computations were obtained for a Rayleigh number range of 10 to 10^4, a radius ratio of 2, an aspect ratio of 1 and a Prandtl number of 0·703. The mean Nusselt numbers computed by the present numerical scheme were in good agreement with those of Schwab and DeWitt.[17] The comparison is shown graphically in Figure 4. Unlike the present numerical scheme, in which the full three-dimensional equations were solved, Schwab and DeWitt[17] took advantage

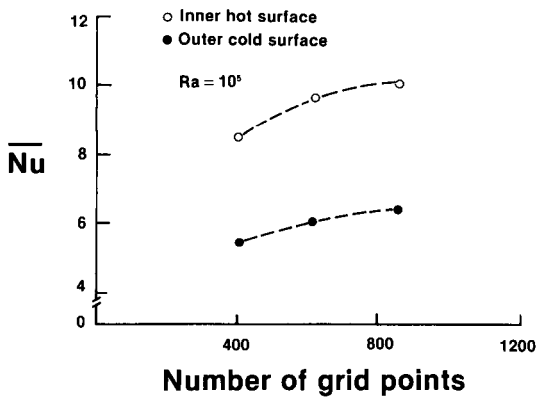

Figure 3. Effect of grid distribution on average Nusselt number

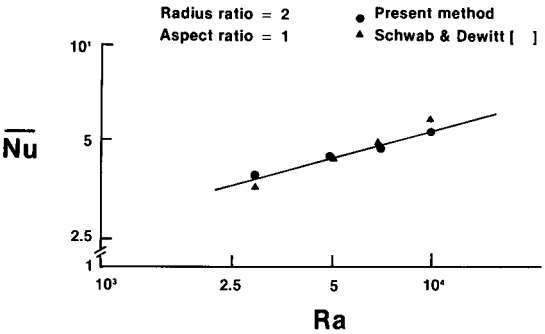

Figure 4. Comparison of Nusselt numbers with previous data: radius ratio = 2, aspect ratio = 1. ● present method; ▲ Schwab and Dewitt[17]

of the axisymmetrical nature of the problem and solved only the two-dimensional governing equations. Further discussion of the computed flow and temperature fields as well as the heat transfer data in the form of Nusselt numbers, is presented in the following sections.

Temperature field

Plots of isotherms for Rayleigh numbers up to 10^6 at various axial and angular positions are shown in Figures 5–9. By defining a new temperature variable $T^* = (T - T_c)/(T_h - T_c)$, the outer boundary temperature is shown as $T^* = 0$ and the inner boundary temperature as $T^* = 1$. To facilitate comparisons, the number of isotherms plotted is kept at 11 for each Rayleigh number considered. The temperature increment between isotherms is also kept uniform at 0·1. For Rayleigh numbers less than 10^3, the isotherms at selected axial planes are evenly distributed between the maximum and minimize temperatures. This demonstrates that the effect of convection is practically negligible at these Rayleigh numbers and that the predominant mode of heat transfer is by conduction. At Reyleigh numbers greater than 10^3, enhanced crowding of isotherms near the inner boundary is observed, indicating the development of the thermal boundary layer. As the Rayleigh number increases beyond 10^3, the temperature gradient becomes steeper and the boundary layer grows thinner. It is also observed that the thermal boundary layer develops closer to the inner boundary near the bottom of the configuration (Figures 5 and 6) and closer to the outer boundary near the top of the enclosure (Figure 7).

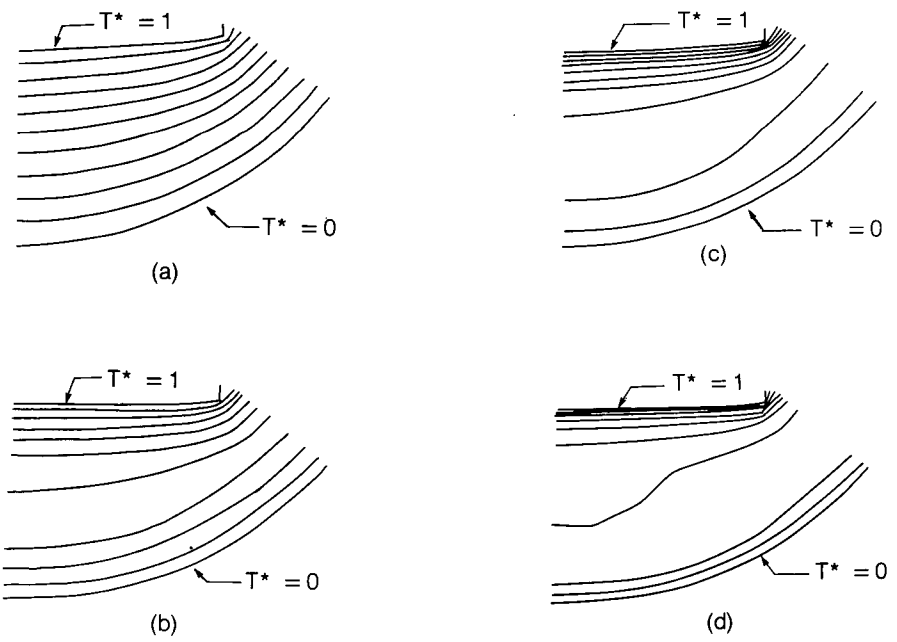

Figure 5. Dimensionless isotherms at a selected axial level: $z = 0{\cdot}834$, $\Delta T^* = 0{\cdot}1$; (a) $Ra = 10^3$, (b) $Ra = 10^4$, (c) $Ra = 10^5$, (d) $Ra = 10^6$

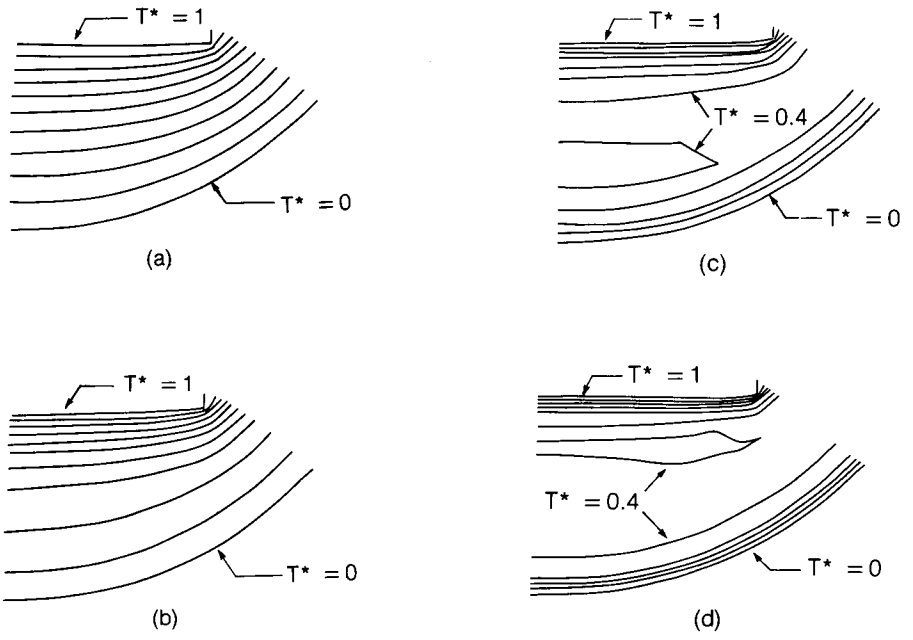

Figure 6. Dimensionless isotherms at a selected axial level: $z = 0{\cdot}4167$, $\Delta T^* = 0{\cdot}1$; (a) $Ra = 10^3$, (b) $Ra = 10^4$, (c) $Ra = 10^5$, (d) $Ra = 10^6$

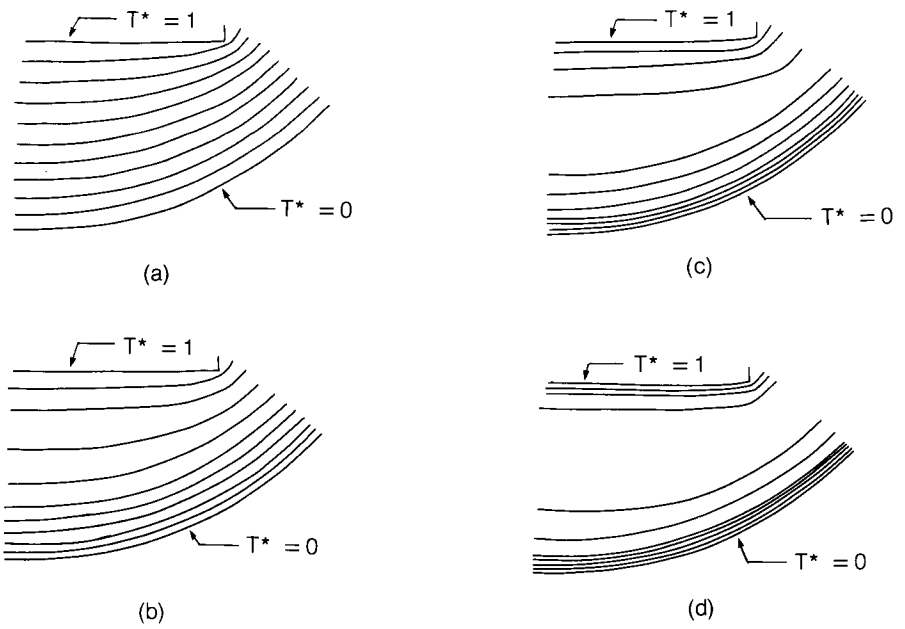

Figure 7. Dimensionless isotherms at a selected axial level: $z = 0{\cdot}9164$, $\Delta T^* = 0{\cdot}1$; (a) $Ra = 10^3$, (b) $Ra = 10^4$, (c) $Ra = 10^5$, (d) $Ra = 10^6$

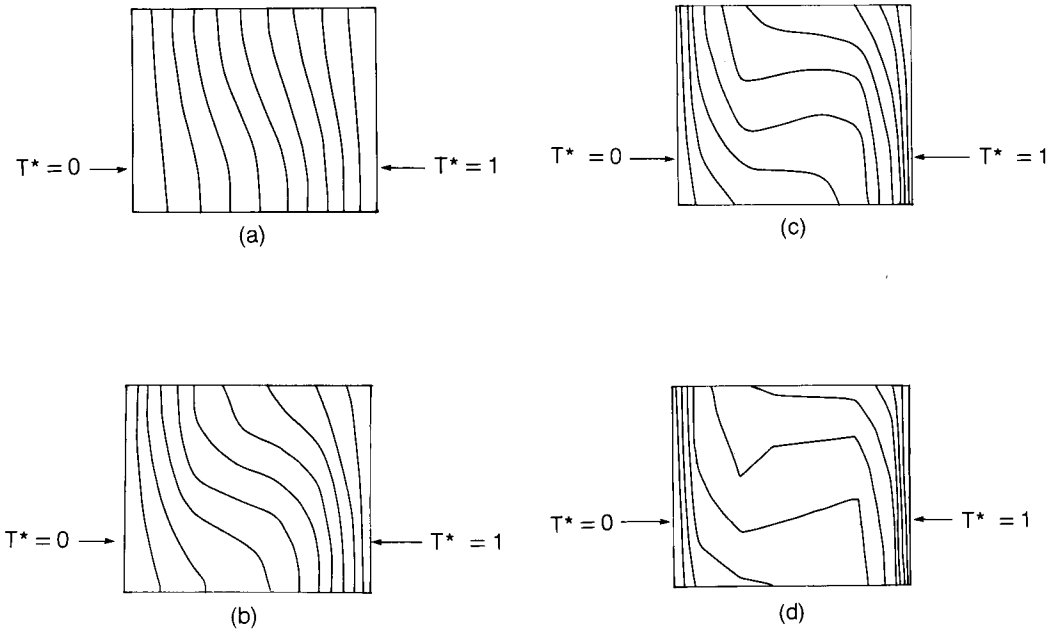

Figure 8. Dimensionless isotherms at a selected angular plane: $x = 0{\cdot}0834$, $\Delta T^* = 0{\cdot}1$; (a) $Ra = 10^3$, (b) $Ra = 10^4$, (c) $Ra = 10^5$, (d) $Ra = 10^6$

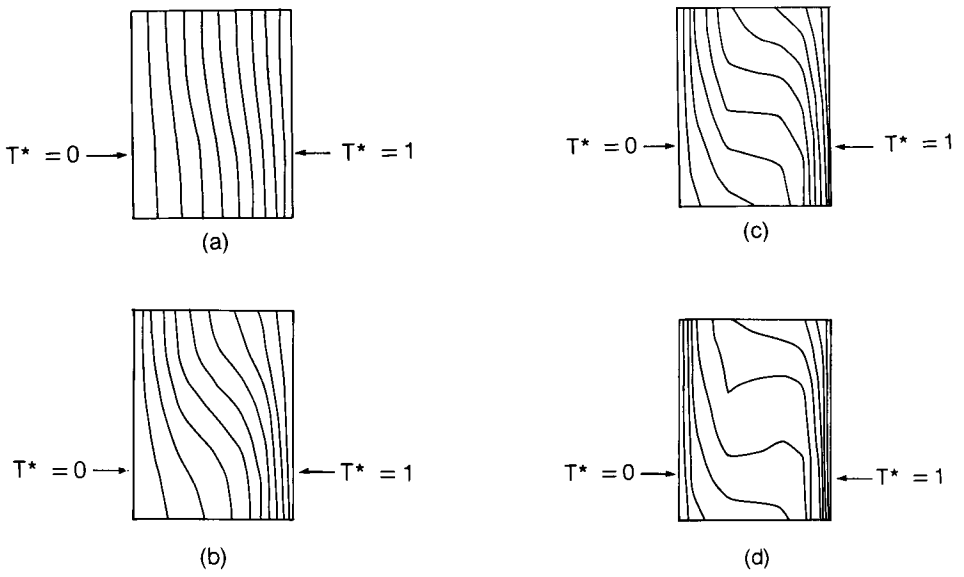

Figure 9. Dimensionless isotherms at a selected angular plane: $x = 0{\cdot}9167$, $\Delta T^* = 0{\cdot}1$; (a) $Ra = 10^3$, (b) $Ra = 10^4$, (c) $Ra = 10^5$, (d) $Ra = 10^6$

Similar conclusions can be drawn by examining the isotherm plots (Figures 8 and 9) for selected angular positions about the vertical axis of the configuration. Each such angular plane is identified by a distance x measured from the symmetry line 0–y (Figure 2). The plots of isotherms in the angular planes show remarkable deviations from the conduction patterns for Rayleigh numbers greater than 10^3. The transition from conduction to mostly convection appears to occur for a Rayleigh number between 10^3 and 10^4. The crowding of isotherms in the vicinity of the inner and outer walls, suggesting the development of boundary layers for higher Rayleigh numbers, is observed in Figures 8 and 9. Similar observations about the conduction, transition and boundary-layer regimes have been reported by at least one other investigator.[20] A variation in the development of the boundary layer on the inner wall is observed from the bottom to the top of the configuration. This is partly due to the presence of horizontal adiabatic surfaces, and the mixing of hot and cold fluid near the top of the enclosure. A similar phenomenon is observed for the boundary layer development on the cold wall.

The appearance of temperature inversions in the isotherm plots (Figures 8 and 9) is a characteristic of natural convection phenomena. The existence of secondary maximum and minimum temperature fields between the hot and cold walls is indicative of these inversions. In the present study, the temperature inversions are observed for Rayleigh numbers greater than 5×10^4. The comparison of isotherms at different angular planes at a Rayleigh number of 10^5 reveals that the gap size between the inner square and the outer cylinder has an influence on the strength of the convection phenomenon. It is observed (Figures 8 and 9) that the temperature inversions are more pronounced at the angular position $x = 0{\cdot}0834$ than at the position $x = 0{\cdot}9167$, which is close to the corner of the inner square rod.

Flow field

To obtain information about the flow structure, plots of velocity vectors for Rayleigh numbers 10^3 to 10^6 at selected axial and angular planes are presented in Figures 10 –14. From the plots of

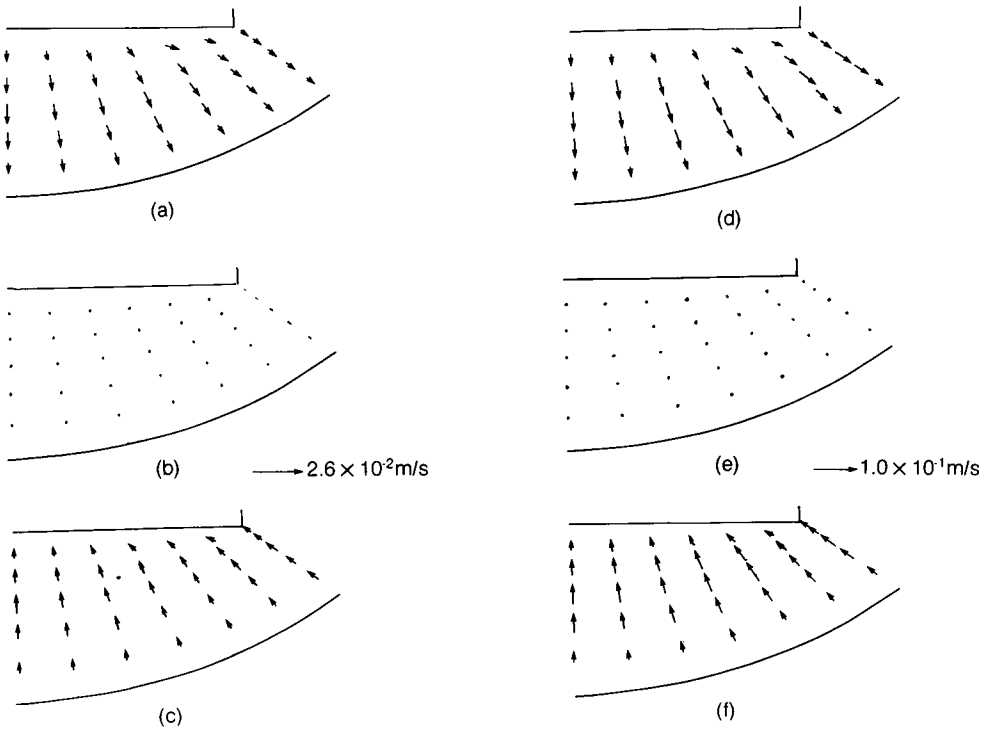

Figure 10. Plots of velocity at selected axial planes. $Ra = 10^3$: (a) $z = 0{\cdot}8333$, (b) $z = 0{\cdot}5$, (c) $z = 0{\cdot}1667$: $Ra = 10^4$: (d) $z = 0{\cdot}8333$, (e) $z = 0{\cdot}5$, (f) $z = 0{\cdot}1667$

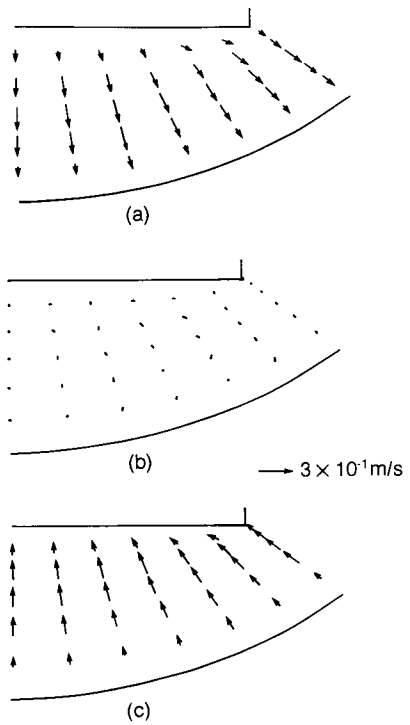

Figure 11. Plots of velocity at selected axial planes. $Ra = 10^5$: (a) $z = 0{\cdot}8333$, (b) $z = 0{\cdot}5$, (c) $z = 0{\cdot}1667$

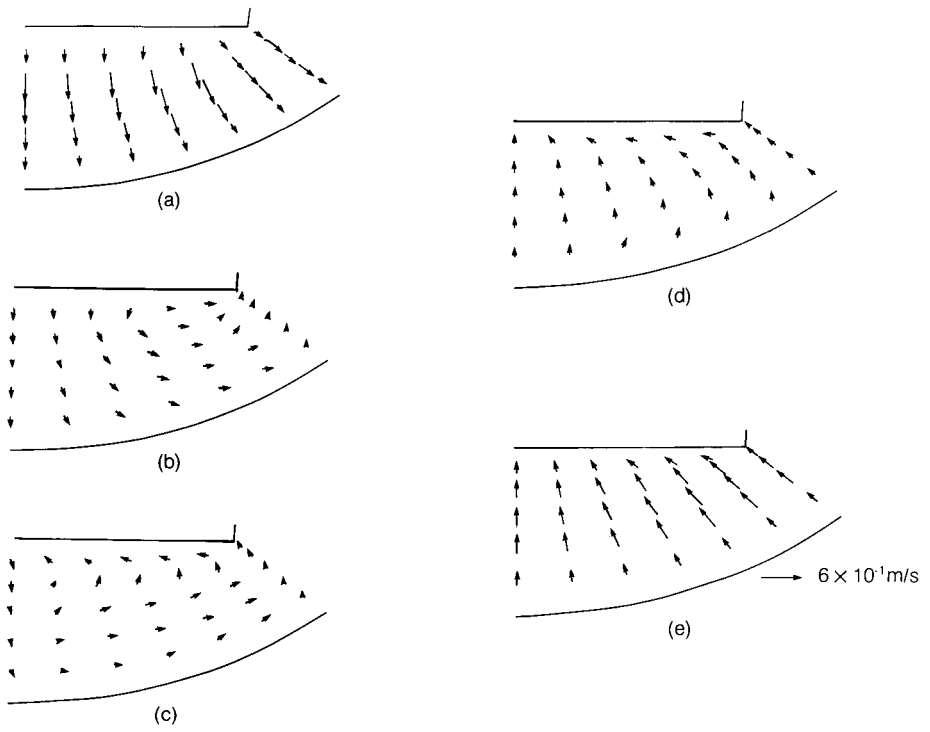

Figure 12. Plots of velocity at selected axial levels. $Ra = 10^6$: (a) $z = 0{\cdot}8333$, (b) $z = 0{\cdot}6667$, (c) $z = 0{\cdot}5$, (d) $z = 0{\cdot}3333$, (e) $z = 0{\cdot}1667$

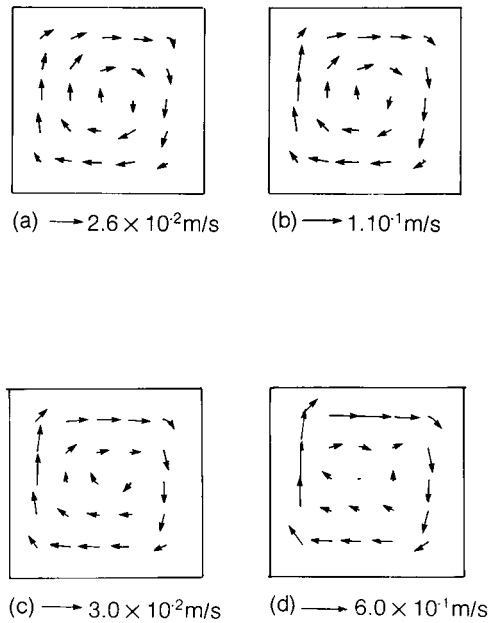

Figure 13. Plots of velocity at a selected angular plane. $x = 0{\cdot}0$: $Ra = 10^3$, (b) $Ra = 10^4$, (c) $Ra = 10^5$, (d) $Ra = 10^6$

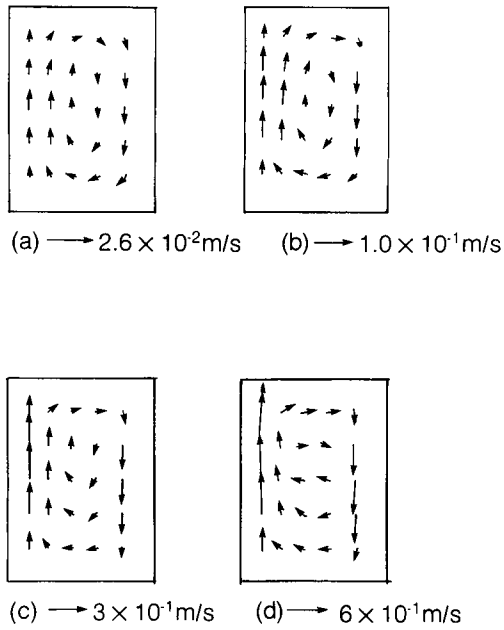

Figure 14. Plots of velocity at a selected angular plane. $x = 0{\cdot}8333$: (a) $Ra = 10^3$, (b) $Ra = 10^4$, (c) $Ra = 10^5$, (d) $Ra = 10^6$

the resultant planar velocity (V_{2D}) in Figures 10–12, it can be inferred that the direction of fluid flow is towards the hot wall near the bottom of the cavity and in the opposite direction near the top of the enclosure. The resultant planar velocity changes direction through 180° as the fluid moves along the axial direction, attaining close to zero values at approximately $z = 0{\cdot}5$ for Rayleigh numbers less than 10^6.

Further inferences about the hydrodynamic boundary layer variation with Rayleigh number can be drawn from Figures 13 and 14. The development of the boundary layer is clearly shown. At each Rayleigh number the velocity increases from zero at the walls, reaches a maximum value and decreases to an almost stagnant region in the middle of the enclosure. The maximum velocity increases with increasing Rayleigh number. In contrast to the results of Davis and Thomas, [18] no flow reversals are observed in the range of Rayleigh numbers studied, resulting in unicellular fluid motion in the cavity. This difference in flow patterns may be due to the low aspect and radius ratios, and the difference in geometrical configurations of the two studies.

Overall heat transfer results

The heat transfer parameter of greatest practical interest is the Nusselt number, defined as the ratio of convection heat transfer to conduction in a fluid slab of thickness equal to the reference length. Since the problem under study is three dimensional in nature, the local Nusselt number is a function of both axial and angular positions on the solid surfaces. A typical variation of the local Nusselt number in the enclosure of interest for $Ra = 5 \times 10^4$ is shown in Figure 15 for the inner surface.

The horizontal average Nusselt number $\overline{Nu}_H$, at an axial level is defined as

$$\overline{Nu}_H = \frac{1}{\xi} \int_0^{\xi_1} Nu(\xi, \zeta = \text{constant})\, d\xi$$

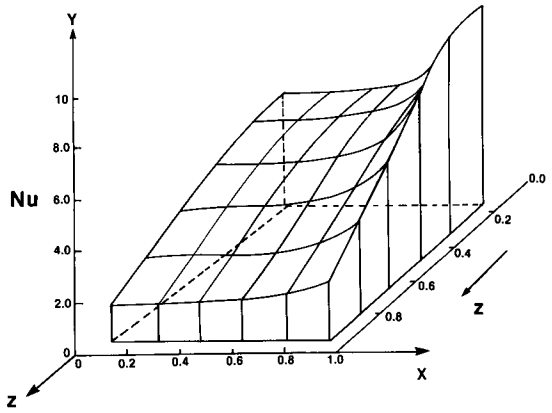

Figure 15. Distribution of local Nusselt number on the inner surface: $Ra = 5 \times 10^4$

and the vertical average Nusselt number $\overline{Nu}_V$ is similarly defined as

$$\overline{Nu}_V = \frac{1}{\zeta} \int_0^{\zeta_1} Nu(\xi = \text{constant}, \zeta)\, d\zeta.$$

The overall (total) average Nusselt number $\overline{Nu}$ is obtained by evaluating the double integral given by

$$\overline{Nu} = \frac{1}{\xi_1 \zeta_1} \int_0^{\xi_1} \int_0^{\zeta_1} Nu(\xi, \zeta)\, d\xi\, d\zeta,$$

where the local Nusselt number $Nu(\xi, \zeta)$ is defined by the relationship

$$Nu(\xi, \zeta) = qL/k(T_w - T_0).$$

With these definitions, the variations of $\overline{Nu}_H$ and $\overline{Nu}_V$ with Rayleigh number for both inner and outer walls are presented in Figures 16 and 17. Examination of Figure 16 shows that $\overline{Nu}_H$ decreases slightly with increasing Rayleigh number up to 5×10^3 near the top of the cavity on the inner boundary. A similar observation for $\overline{Nu}_H$ is made for the outer boundary but at the bottom of the enclosure. Similar to the observations made by Davis and Thomas,[18] the $\overline{Nu}_H$ variation achieves higher values near the bottom of the cavity for Rayleigh numbers higher than 10^3 on the inner boundary (Figure 16). The trend is the reverse on the outer boundary where $\overline{Nu}_H$ attains asymptotic values at the top of the enclosure. The presence of the corner on the inner body is found to increase the average vertical Nusselt number $\overline{Nu}_V$; however, there is little variation in $\overline{Nu}_V$ on the cold surface (Figure 17).

The total average Nusselt number $\overline{Nu}$ variation with Rayleigh number is presented in Figure 18 for both the inner and outer boundaries. From these plots, three distinct regions of heat transfer can be determined. These are the conduction region for $0 \leqslant Ra < 10^3$; the transition region for $10^3 \leqslant Ra < 5 \times 10^3$ and the laminar boundary layer region that prevails in the Rayleigh number range of 5×10^3 to 10^6.

CONCLUSION

Numerical results have been obtained, yielding for the first time information about the three-dimensional motion and heat transfer due to natural convection occurring in a vertical enclosure

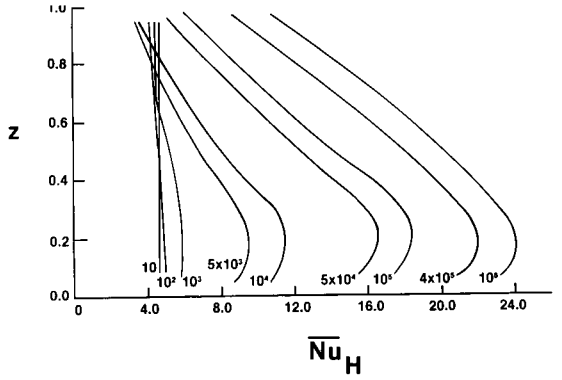

Figure 16(a). Variation of $\overline{Nu}_H$ on inner surface as a function of axial distance

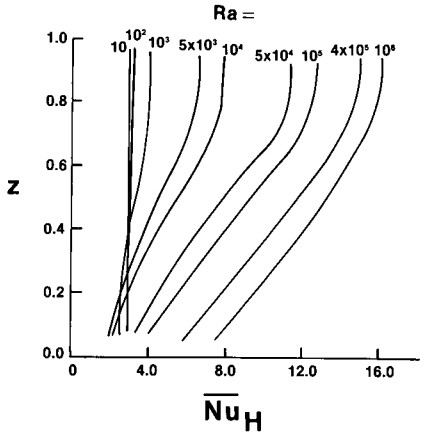

Figure 16(b). Variation of $\overline{Nu}_H$ on outer surface as a function of axial distance

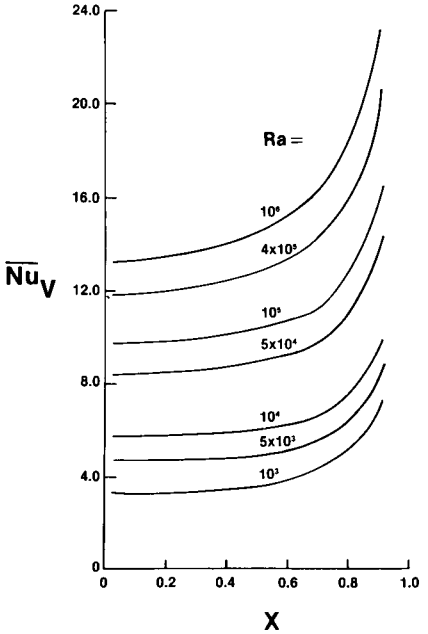

Figure 17(a). Lateral variation of Nu_V on inner surface

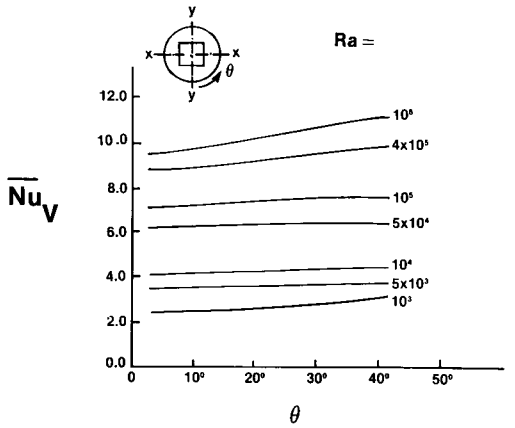

Figure 17(b). Lateral variation of $\overline{Nu}_V$ on outer surface

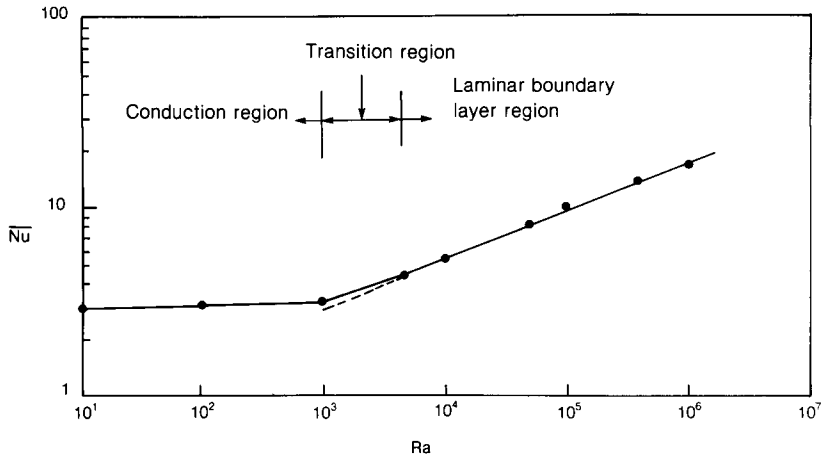

Figure 18(a). Variation of inner body average Nusselt number as a function of Rayleigh number

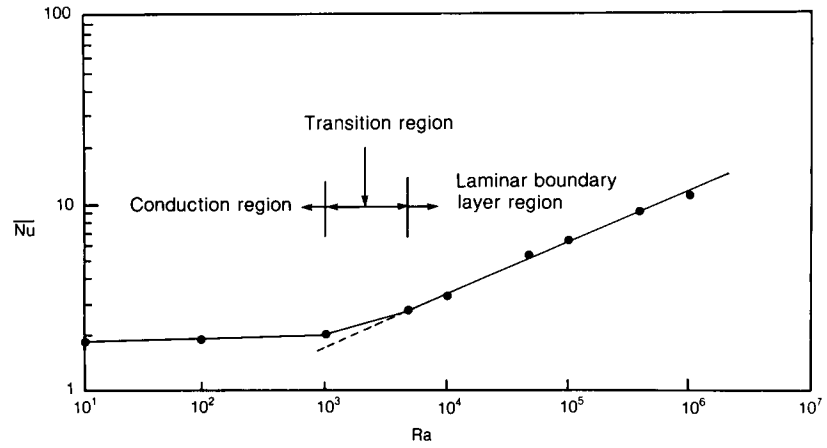

Figure 18(b). Variation of outer body average Nusselt number as a function of Rayleigh number

formed by a square rod inside a concentric cylinder. The computations required modification and extension of a previously developed numerical scheme. Test calculations to verify the modified numerical scheme have produced results that compare favourably with published results.

For the enclosure geometry of interest, results have been obtained for air ($Pr = 0{\cdot}703$) in the Rayleigh number range of 0 to 10^6 where the aspect and radius ratios were kept fixed at 1. The results show that details of the flow and the Nusselt number depend upon the Rayleigh number. For all the Rayleigh number results obtained, unicellular flow patterns were observed to occur in the enclosure. The distribution of the derived heat transfer data on the inner boundary revealed that the local Nusselt number attains its highest value near the bottom of the enclosure close to the inner corner region. From the distribution of the total average Nusselt number with Rayleigh number, the heat transfer results can be correlated in the form $\overline{Nu} = \text{constant} \times Ra^m$. These correlations are

$$\overline{Nu} = 2{\cdot}816 Ra^{0{\cdot}016} \text{(inner wall)},$$
$$\overline{Nu} = 1{\cdot}795 Ra^{0{\cdot}016} \text{(outer wall)},$$

in the conduction region, and.

$$\overline{Nu} = 0{\cdot}470 Ra^{0{\cdot}263} \text{(inner wall)},$$
$$\overline{Nu} = 0{\cdot}302 Ra^{0{\cdot}262} \text{(outer wall)},$$

in the laminar boundary layer region. These correlations are found to predict the original data to within a difference of less than five per cent.

ACKNOWLEDGEMENT

We gratefully acknowledge the support of the U.S. Nuclear Regulatory Commisssion and U.S. Department of Energy under grant numbers NRC-G-04-81-007 and DE-FG05-840R21495.

NOMENCLATURE

a	a positive constant prescribing the linear transformation in the z direction
b	side of square rod
c_p	specific heat at constant pressure
D	outer cylinder diameter
g	acceleration due to gravity
h	dimensionless specific enthalpy $= \bar{h}/h_0$; an overbar denotes a dimensional quantity
H	height of enclosure
IMAX, JMAX, KMAX	grid distribution in ξ, η, ζ directions
J, J_{12}	Jacobians of transformation
k	thermal conductivity
L	reference length $= (D - b)/2$
Nu	local Nusselt number based on maximum gap width
$\overline{Nu}$	average Nusselt number
$\overline{Nu}_V$	average Nusselt number along a constant vertical line
$\overline{Nu}_H$	average Nusselt number along a constant horizontal line
p	dimensionless pressure $= (\bar{p} - \bar{p}_s)/\rho_0 V_0^2$
p'	pressure-correction
Pr	Prandtl number
q	heat flux in physical geometry
$\tilde{q}$	dimensionless heat flux in transformed geometry
Ra	Rayleigh number $= g\beta L^3(T_h - T_c)Pr/\nu^2$
t	dimensionless time $= \bar{t}V_0/L$
T	dimensionless temperature $= \bar{T}c_{p0}/h_0$
u, v, w	dimensionless components of velocity in the physical geometry
$\tilde{u}, \tilde{v}, \tilde{w}$	ξ, η and ζ components of velocity in the transformed geometry
V_0	reference velocity $= \nu/L$
x, y, z	Cartesian co-ordinate directions
α, β, γ	transformation coefficients
θ, ω, ψ	angular positions
ξ, η, ζ	co-ordinate directions in the transformed geometry
ρ	density

ν	kinematic viscosity
β	volumetric coefficient of thermal expansion
$\tilde{\Sigma}$	dimensionless shear stress in transformed co-ordinates

Subscripts

c, h	outer and inner surfaces
i, j, k	indices for grid points
0	reference quantity
ξ, η, ζ, t	first partial derivatives
s	static value
w	wall value

REFERENCES

1. T. H. Kuehn and R. J. Goldstein, 'An experimental and theoretical study of natural convection in the annulus between horizontal concentric cylinders', *Journal of Fluid Mechanics*, **74,** 695–719 (1976).
2. K. Aziz and J. D. Hellums, 'Numerical solution of the three-dimensional equations of motion for laminar natural convection', *The Physics of Fluids*, **10** (2), 314–324 (1967).
3. G. D. Mallinson and G. De Vahl Davis, 'The method of false transient for the solution of coupled elliptic equations', *Journal of computational Physics*, **12,** 434–461 (1973).
4. G. D. Mallinson and G. De Vahl Davis, 'Three-dimensional natural convection in a box: A numerical study', *Journal of Fluid Mechanics*, **83,** part 1, 1–31 (1977).
5. H. Ozoe, K. Yamamoto, H. Sayama and S. W. Churchill, 'Natural convection patterns in a long inclined rectangular box heated from below', *Int. J. Heat Mass Transfer*, **20,** 131–139 (1977).
6. A. M. C. Chan and S. Banerjee, 'Three-dimensional numerical analysis of transient natural convection in rectangular enclosures', *ASME Journal of Heat Transfer*, **101,** 114–119 (1979).
7. F. H. Harlow and J. E. Welch, 'Numerical calculation of time-dependent viscous incompressible flow of fluid with free surface', *Physics of Fluids*, **8** (12), 2182–2189 (1965).
8. Y. Takata, K. Fukuda, S. Hasegawa and K. Iwashige, 'Three-dimensional natural convection in a porous medium enclosed in a vertical curved annulus', *Numerical Heat Transfer*, **6,** 29–39 (1983).
9. Y. Takata, K. Iwashige, K. Fukuda and S. Hasegawa, 'Three-dimensional natural convection in an inclined cylindrical annulus', *Int. J. Heat mass Transfer*, **27** (5), 747–754 (1984).
10. A. K. Tolpadi and T. H. Kuehn, 'Conjugate three-dimensional natural convection heat transfer from a horizontal cylinder with long Transverse plate fins', *Numerical Heat Transfer*, **7,** 319–341 (1984).
11. B. C. J. Chen, W. T. Sha, M. L. Doria, R. C. Schmitt and J. F. Thompson, 'BODYFIT-1FE: a computer code for three-dimensional steady state/transient single-phase rod-bundle thermal hydraulic analysis', NUREG/CR-1874, ANL-80-127, November 1980.
12. E. K. Glakpe, C. B. Watkins and J. N. Cannon, 'Natural convection solutions-between concentric and eccentric horizontal cylinders with specified heat flux boundaries', *Heat Transfer in Enclosures, ASME HTD*, **39,** 79–86 (1984).
13. J. F. Thompson, *Numerical Grid Generation*, Elsevier Science Publishing Co. Inc., 1982.
14. P. J. Roache, *Computational Fluid Dynamics*, Hermosa Publishers, 1982.
15. S. V. Patankar, *Numerical Heat Transfer and Fluid Flow*, Hemisphere Publishing Corporation, 1980.
16. B. Kurien, 'Three-dimensional computations of natural convection inside a vertical enclosure', *M. S. Thesis*, Howard University, Washington, D. C., 1984.
17. T. H. Schwab and K. J. DeWitt, 'Numerical investigation of free convection between two vertical coaxial cylinders', *AIChE Journal*, **16** (6), 1005–1010 (1970).
18. G. De Vahl Davis and R. W. Thomas, 'Natural convection between concentric vertical cylinders', *High Speed Computing in Fluid Dynamics, The Physics of Fluids Supplements, II* 1969, pp. II 198–II 207.
19. R. W. Thomas and G. De Vahl Davis, 'Natural convection in annular and rectangular cavities. A numerical study', *Proceedings, Fourth International Heat Transfer Conference*, Paris, Vol. 4, Paper NC 2.4, Elsevier, Amsterdam, 1970.
20. B. Farouk and S. I. Guceri, 'Laminar and turbulent natural convection heat transfer in the annulus betwen horizontal concentric cylinders', *Journal of Heat Transfer*, **104,** 631–636 (1982).